Ishiyama et al. *NPG Asia Materials* (2024)16:17
https://doi.org/10.1038/s41427-024-00536-w

NPG Asia Materials

ARTICLE Open Access

Bayesian optimization-driven enhancement of the thermoelectric properties of polycrystalline III-V semiconductor thin films

Takamitsu Ishiyama[1], Koki Nozawa[1], Takeshi Nishida[2], Takashi Suemasu[1] and Kaoru Toko[1]

Abstract

Studying the properties of thermoelectric materials needs substantial effort owing to the interplay of the trade-off relationships among the influential parameters. In view of this issue, artificial intelligence has recently been used to investigate and optimize thermoelectric materials. Here, we used Bayesian optimization to improve the thermoelectric properties of multicomponent III–V materials; this domain warrants comprehensive investigation due to the need to simultaneously control multiple parameters. We designated the figure of merit *ZT* as the objective function to improve and search for a five-dimensional space comprising the composition of InGaAsSb thin films, dopant concentration, and film-deposition temperatures. After six Bayesian optimization cycles, *ZT* exhibited an approximately threefold improvement compared to its values obtained in the random initial experimental trials. Additional analysis employing Gaussian process regression elucidated that a high In composition and low substrate temperature were particularly effective at increasing *ZT*. The optimal substrate temperature (205 °C) demonstrated the potential for depositing InGaAsSb thermoelectric thin films onto plastic substrates. These findings not only promote the development of thermoelectric devices based on III–V semiconductors but also highlight the effectiveness of using Bayesian optimization for multicomponent materials.

Introduction

Thermoelectric generators have attracted considerable interest owing to the increasing demand for energy harvesting technologies[1,2]. In particular, flexible thermoelectric devices that can be deployed in diverse environments have significant potential for internet of things applications, such as remote sensing[3–6]. The figure of merit (ZT) of a thermoelectric device is a measure of its heat-to-electricity conversion performance. It is expressed as $ZT = \sigma S^2 T \kappa^{-1} = PF \kappa^{-1}$, where σ, S, κ, PF, and T denote the electrical conductivity, Seebeck coefficient, thermal conductivity, power factor, and ambient temperature, respectively. Each parameter is influenced by the carrier density and scattering factors (phonon scattering, alloy scattering, etc.), creating a trade-off relationship among these parameters[7–11]. Consequently, when the ZT of a material is increased, its electronic and thermal transport properties need to be optimized. Narrow bandgap III–V compound semiconductors are promising candidates for achieving thermoelectric thin films that utilize micro-energy near room temperature (RT)[12–15]. However, the performance optimization of the III–V compound semiconductors needs considerable effort because of their large number of possible combinations[16–19].

Recently, several innovative techniques have been developed based on machine learning; these techniques include high-dimensional-parameter search techniques such as Bayesian optimization (BO)[20–25]. The efficacy of BO has been demonstrated with thin-film thermoelectric materials such as Bi_2Te_3[26–31]. BO may be particularly effective for multicomponent thermoelectric thin films with many parameters. Group III–V compound semiconductors are receiving

Correspondence: Kaoru Toko (toko@bk.tsukuba.ac.jp)
[1]Institute of Applied Physics, University of Tsukuba, 1-1-1 Tennodai, Tsukuba, Ibaraki 305-8573, Japan
[2]Global Zero Emission Research Center, AIST, 1-1-1 Umezono, Tsukuba, Ibaraki 305-8568, Japan

Fig. 1 Schematic of the experimental cycles. The following cycle is repeated: (i) thin-film deposition, (ii) thermoelectric property measurements, and (iii) BO recommendations.

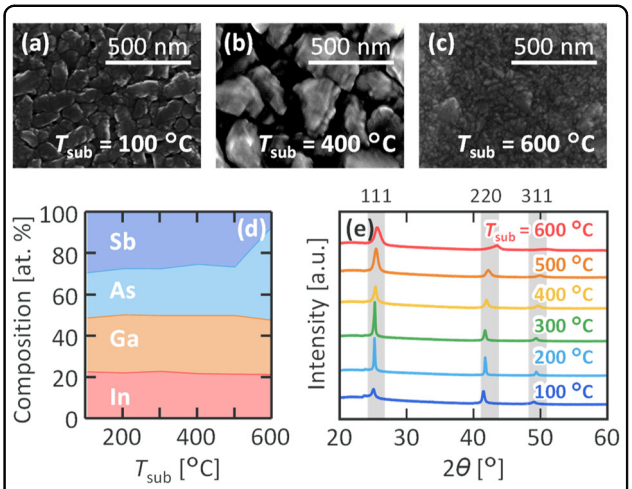

Fig. 2 Crystal properties of the undoped InGaAsSb films. Scanning electron micrographs of the crystal at T_{sub} = (**a**) 100 °C, (**b**) 400 °C, and (**c**) 600 °C. (**d**) Composition ratio obtained from EDX analysis and (**e**) out-of-plane XRD patterns for T_{sub} = 100–600 °C. The gray areas indicate the peak positions corresponding to the 111, 220, and 311 orientations of the InGaAsSb crystal. The cell temperatures were fixed at $T_{Ga\text{-}cell}$ = 977 °C, $T_{As\text{-}cell}$ = 255 °C, and $T_{Sb\text{-}cell}$ = 430 °C.

increased attention mainly as single-crystal materials; however, from the perspective of thermoelectric applications, polycrystalline materials are preferable because they can utilize phonon scattering. Reports on the polycrystalline III–V compound thin films are limited but indicate that these compounds can be formed at relatively low temperatures[32–36]. These results indicate the possibility of fabricating a plastic-film-based III–V compound thermoelectric film. In this study, we propose a BO-based *ZT* optimization approach, focusing on Sn-doped polycrystalline $In_{1-x}Ga_xAs_{1-y}Sb_y$ thin films. These films provide a large search space with modifiable crystal and transport properties. We succeeded in improving *ZT* by nearly three times with only six cycles. Furthermore, we elucidated the pivotal guidelines for improving the *ZT* of the polycrystalline InGaAsSb thin films.

Results

Figure 1 shows a schematic diagram of the experimental cycle used in this study. The BO model learns the relationship between the previous experimental conditions and objective values and then predicts new experimental conditions that can lead to the highest degree of improvement. We repeated the following cycles: (i) thin-film deposition, (ii) thermoelectric property measurements, and (iii) BO recommendations.

Figure 2 shows the influence of the substrate temperature (T_{sub}) on the crystallinity of $In_{1-x}Ga_xAs_{1-y}Sb_y$ films not doped with Sn. The Ga-cell temperature ($T_{Ga\text{-}cell}$), As-cell temperature ($T_{As\text{-}cell}$), and Sb-cell temperature ($T_{Sb\text{-}cell}$) were set as 977 °C, 255 °C, and 430 °C, respectively, and the Sn-cell temperature ($T_{Sn\text{-}cell}$) was set to RT. These cell temperatures corresponded to those that yield approximately $x = y = 0.5$ at T_{sub} = 400 °C. As shown in the scanning electron microscopy (SEM) images in Fig. 2a–c, the surface morphology of the samples depended on T_{sub}. As T_{sub} varied, the grain size of the samples varied, ranging from approximately 100 nm to 500 nm. According to the energy dispersive X-ray (EDX) mapping, the composition of $In_{1-x}Ga_xAs_{1-y}Sb_y$ was uniform in these SEM images (Supplementary Fig. S1). We derived the composition ratio from the EDX spectra obtained from the samples. As shown in Fig. 2d, for $T_{sub} \leq 500$ °C, the composition of $In_{1-x}Ga_xAs_{1-y}Sb_y$ remained largely consistent at $x = y = 0.5$. However, at T_{sub} = 600 °C, the proportion of Sb decreased. These results indicated that Sb tended to evaporate at high temperatures, with the resulting deficiency compensated by As. As shown in Fig. 2e, all samples exhibited three X-ray diffraction (XRD) patterns corresponding to polycrystalline InGaAsSb. Crystallization at temperatures as low as 100 °C is highly conducive to the development of the III–V compound films on plastic films[29–31]. The peaks shifted to higher angles as T_{sub} increased, which was attributed to the decrease in the lattice constant, likely due to the compositional changes in $In_{1-x}Ga_xAs_{1-y}Sb_y$. Therefore, not only cell temperature but also T_{sub} influenced the composition of $In_{1-x}Ga_xAs_{1-y}Sb_y$ films, complicating the manual optimization of the experimental conditions.

Figure 3a, b shows the electrical and thermoelectric characteristics of the samples discussed above. As shown

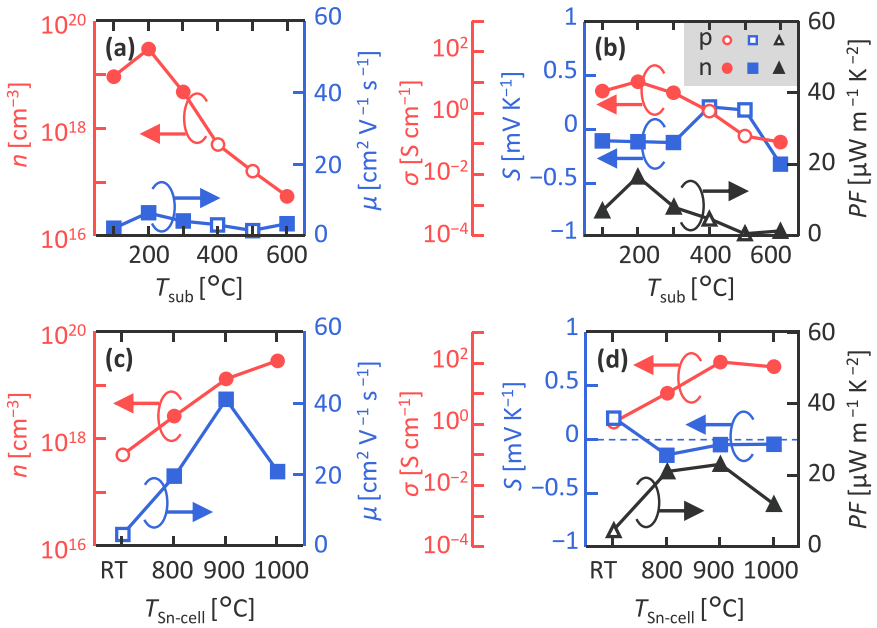

Fig. 3 Electrical and thermoelectrical properties of the InGaAsSb films. The influence of T_{sub} on (**a**) n and μ and (**b**) σ, S, and PF of the samples fabricated without Sn addition. The influence of the $T_{Sn\text{-}cell}$ on (**c**) n and μ and (**d**) σ, S, and PF at $T_{sub} = 400$ °C. The cell temperatures were fixed at $T_{Ga\text{-}cell} = 977$ °C, $T_{As\text{-}cell} = 255$ °C, and $T_{Sb\text{-}cell} = 430$ °C. The open and closed symbols denote p-type and n-type conduction, respectively, as shown in the inset in **b**.

in Fig. 3a, the carrier concentration (n) significantly depends on T_{sub}, whereas the mobility (μ) exhibits minimal variations as T_{sub} increases. The crystal exhibits p-type behaviors at $T_{sub} = 400$ °C and 500 °C and n-type behaviors at all other temperatures. This reflects the behavior of the InAs–GaSb alloy, where InAs and GaSb are generally n-type and p-type semiconductors, respectively, at RT[37,38]. Considering the above results and the findings shown in Fig. 2d, the dependence of the conductivity type on T_{sub} can be elucidated as follows: at $T_{sub} = 200$ °C and 300 °C, the n-type InAs dominate the conductivity; at $T_{sub} = 400$ °C and 500 °C, partial replacement of InAs by GaSb results in a p-type conductivity; and at $T_{sub} = 600$ °C, Sb evaporates, causing the n-type InAs formation to dominate once again. As shown in Fig. 3b, the sign of S, which indicates the conductivity type, is consistent with the Hall effect measurement results. σ and PF reflect the behavior of n reaches a maximum at $T_{sub} = 200$ °C. Figure 3c, d shows the influence of the $T_{Sn\text{-}cell}$ on the electrical and thermoelectric characteristics of the alloy at $T_{sub} = 400$ °C. According to the secondary ion mass spectrometry (SIMS) measurements, the concentrations of Sn in the $In_{1-x}Ga_xAs_{1-y}Sb_y$ films were 7.8×10^{19}, 8.5×10^{20}, and 6.3×10^{21} cm^{-3} at $T_{Sn\text{-}cell} = 800$ °C, 900 °C, and 1000 °C, respectively. As shown in Fig. 3c, all Sn-doped samples exhibit n-type conductivity, where n increases with increasing $T_{Sn\text{-}cell}$. This occurs because Sn acts as a donor in III–V compound semiconductors[39,40]. μ exhibits a peak at $T_{Sn\text{-}cell} = 900$ °C; this peak is typically observed in polycrystalline semiconductor thin films owing to the balance between grain boundaries and impurity scattering. As shown in Fig. 3d, the σ and PF peaks at $T_{Sn\text{-}cell} = 900$ °C reflect the balance between n and μ. In summary, the thermoelectric performance of $In_{1-x}Ga_xAs_{1-y}Sb_y$ thin films depends not only on the elemental composition of the III–V semiconductors but also on the substrate temperature and Sn doping levels. Based on these results, the T_{sub} and $T_{Sn\text{-}cell}$ ranges were set to 100–600 °C and 600–1000 °C, respectively, for the BO of ZT.

We investigated the influence of the $In_{1-x}Ga_xAs_{1-y}Sb_y$ composition on κ. Figure 4 illustrates the dependence of κ on the composition of an Sn-free sample at $T_{sub} = 400$ °C. Compositional alloying decreased κ, which could be reasonably attributed to enhanced alloy scattering. The introduction of In and Sb was particularly effective at reducing κ, which agreed with that they were relatively heavy metallic elements. At $x = y = 0.5$, κ reached a low value of 1.05 W m^{-1} K^{-1}. At $T_{sub} = 100$ °C, the κ of the sample was 0.57 W m^{-1} K^{-1} at $x = y = 0.5$. These results indicated that crystallinity decreased with decreasing T_{sub}, which also decreased κ. In contrast, κ was independent of $T_{Sn\text{-}cell}$ within the experimental conditions of this study. This behavior was consistent with the fact that Sn was added at the doping level. Based on the above findings and previous studies[7,8], we fitted κ to the experimental results

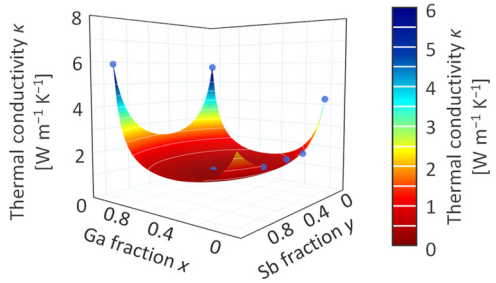

Fig. 4 Influence of the composition of the Sn-free $In_{1-x}Ga_xAs_{1-y}Sb_y$ films on κ at $T_{sub} = 400$ °C. The blue dots represent the measured values, and the curved surface shows the fitting result.

using six parameters (W_{InAs}, W_{GaAs}, W_{InSb}, W_{GaSb}, a, κ_0) as follows:

$$\kappa = [W_{InAs}(1-x)(1-y) + W_{GaAs}(1-x)y + W_{InSb}x(1-y) + W_{GaSb}xy]^{-1} + aT_{sub} + \kappa_0. \quad (1)$$

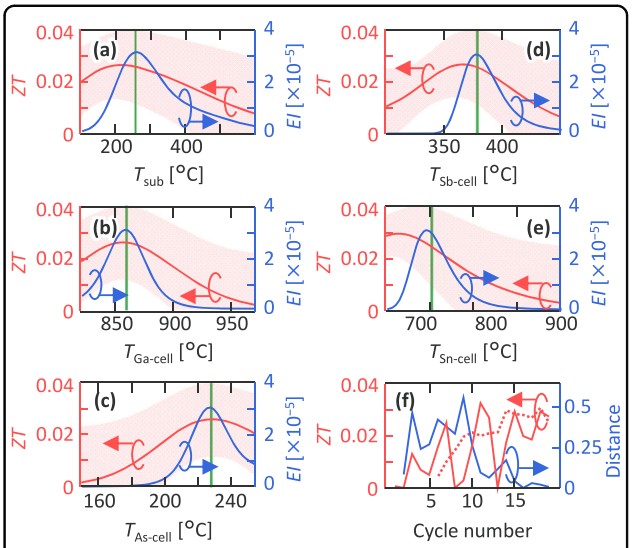

Fig. 5 BO process. a–e Predicted value of ZT (solid red), 95% confidence interval (light red), condition (solid green), and EI (solid blue) at the 19th cycle as a function of (**a**) T_{sub}, (**b**) $T_{Ga\text{-}cell}$, (**c**) $T_{As\text{-}cell}$, (**d**) $T_{Sb\text{-}cell}$, and (**e**) $T_{Sn\text{-}cell}$. **f** ZT (red solid red), ZT_{pred} (red dashed line), and distance (blue solid line) with respect to the number of cycles.

We executed BO using a Gaussian process regression (GPR) algorithm and the characteristics of the samples prepared under five random conditions (1st–5th cycles) within the search range, which were set as the initial points. The next proposed conditions were predicted to lead to the maximum value of the expected improvement (*EI*). Figure 5a–e shows the GPR results from the 19th experiment. The figures show the ZT and EI cutting planes and the next proposed condition; these are 5-parameter functions. In this manner, BO optimizes all five parameters simultaneously, as shown in Table 1. As shown in Fig. 5f, the measured and predicted ZT (ZT_{pred}) increase, and the condition variation distance decreases with increasing cycle number. We defined the condition variation distance as the Euclidean distance between the normalized parameters under the previous and subsequent proposed conditions. The ZT and EI values converged to high and small values, respectively, with large fluctuations (Supplementary Fig. S2). The heatmaps of ZT_{pred} corresponding to cross-sections of two parameters under the experimental conditions clearly showed the areas where high ZT was expected (Supplementary Fig. S3). These results indicated that the BO process converged. All samples in this BO cycle were the n-type. The p-type region was not suitable for thermoelectric applications owing to its significantly low σ; hence, exploring this region using the optimization model was deduced to provide the limited value. At the 11th cycle, the sample exhibited a maximum ZT of 0.033, at which $T_{sub} = 205$ °C, $T_{Ga\text{-}cell} = 860$ °C, $T_{As\text{-}cell} = 220$ °C, $T_{Sb\text{-}cell} = 350$ °C, and $T_{Sn\text{-}cell} = 640$ °C. The sample exhibited a composition of $x = 0.13$ and $y = 0.04$, a Sn concentration of 9.6×10^{18} cm^{-3}, a κ of 1.76 W m^{-1} K^{-1}, and a PF of 150.3 μW m^{-1} K^{-2}. After the 12th cycle, ZT_{pred} and EI exhibited relatively high values, where a finer search in the vicinity of optimal conditions was carried out. As shown in Table 1, among the cell temperatures, the variation in $T_{Sb\text{-}cell}$ was relatively large, which indicated that the other parameters, such as $T_{Ga\text{-}cell}$ and $T_{As\text{-}cell}$, had a more significant influence on ZT. A comparison between the maximum initial points revealed that an approximately threefold improvement in ZT (from an initial value of 0.013) was achieved within only 6 cycles. Notably, BO proposed a low substrate temperature ($T_{sub} = 205$ °C), which could potentially facilitate the deposition of InGaAsSb thermoelectric films on plastic substrates and further expand the applicability of this material.

We systematically organized the sample properties (σ, S, PF, and ZT) as functions of n. As shown in Fig. 6a, b, σ and S increase and decrease, respectively, as n increases. This is a typical behavior exhibited by semiconductor materials. As shown in Fig. 6c, PF has a maximum at approximately $n = 10^{18}$–10^{19} cm^{-3}, reflecting the delicate balance between σ and S. As shown in Fig. 6d, ZT also attains its maximum value in the same n range, reflecting the characteristics of PF. A common challenge with BO is the lack of physical insight into the process of optimizing parameters. Therefore, we analyzed the experimental ZT values in terms of the $In_{1-x}Ga_xAs_{1-y}Sb_y$ composition, T_{sub}, and $T_{Sn\text{-}cell}$. As shown in Fig. 6e, f, achieving a high ZT relies upon three critical factors: a high compositional presence of In and As, low T_{sub},

Table 1 Summary of the parameters used in BO. The predicted values of *ZT* (ZT_{pred}) and *EI*, the BO model outputs, are also shown for each cycle.

Cycle number	T_{sub} [°C]	$T_{Ga\text{-}cell}$ [°C]	$T_{As\text{-}cell}$ [°C]	$T_{Sb\text{-}cell}$ [°C]	$T_{Sn\text{-}cell}$ [°C]	*ZT*	ZT_{pred}	*EI*
1	400	935	205	405	795	0.001		
2	310	960	205	350	830	0.000		
3	130	820	255	410	765	0.013		
4	270	820	235	315	855	0.007		
5	300	940	230	330	830	0.005		
6	585	825	250	300	635	0.016	0.005	2.2×10^{-6}
7	130	885	235	325	605	0.025	0.010	5.3×10^{-6}
8	100	820	150	300	600	0.000	0.015	6.0×10^{-5}
9	100	935	255	380	600	0.003	0.020	3.3×10^{-5}
10	235	845	255	310	600	0.016	0.021	8.5×10^{-5}
11	165	860	220	350	640	0.033	0.020	1.5×10^{-5}
12	350	845	215	365	600	0.027	0.021	1.6×10^{-5}
13	135	840	195	395	600	0.000	0.021	1.3×10^{-5}
14	280	870	220	330	650	0.017	0.030	9.2×10^{-5}
15	205	850	240	365	620	0.029	0.028	1.0×10^{-4}
16	100	850	235	345	675	0.020	0.028	4.9×10^{-5}
17	220	830	225	345	600	0.019	0.027	3.6×10^{-5}
18	215	875	225	365	600	0.029	0.031	6.4×10^{-5}
19	265	855	230	380	690	0.027	0.025	3.0×10^{-5}

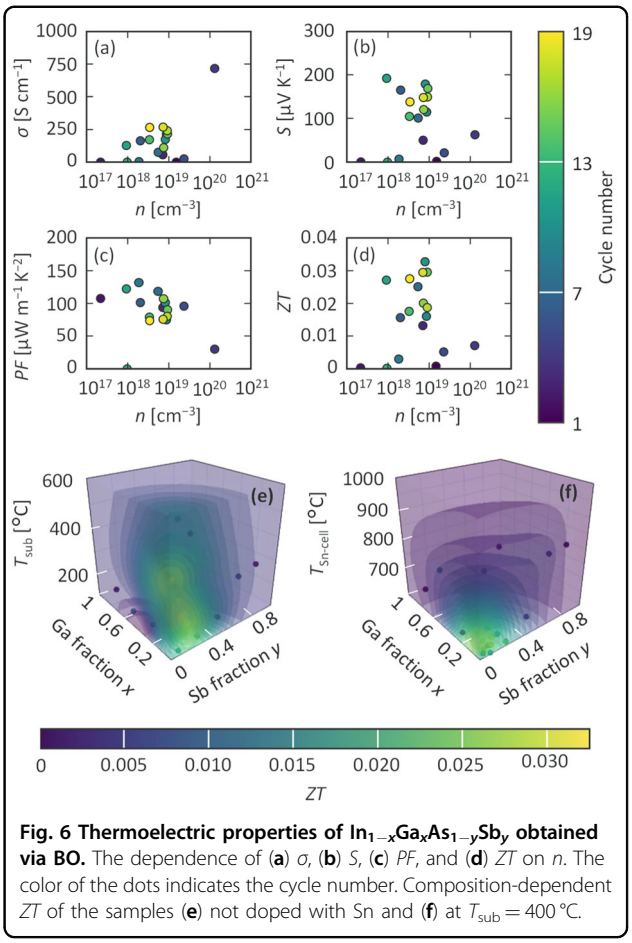

Fig. 6 Thermoelectric properties of $In_{1-x}Ga_xAs_{1-y}Sb_y$ obtained via BO. The dependence of (**a**) *σ*, (**b**) *S*, (**c**) *PF*, and (**d**) *ZT* on *n*. The color of the dots indicates the cycle number. Composition-dependent *ZT* of the samples (**e**) not doped with Sn and (**f**) at $T_{sub} = 400$ °C.

and low $T_{Sn\text{-cell}}$. This behavior can be interpreted as follows. The incorporation of In increases *σ*, and the addition of a modest quantity of Sb coupled with a reduced T_{sub} decreases *κ*. Furthermore, a decrease in $T_{Sn\text{-cell}}$ increases *S*. In reality, the parameters such as *σ*, *S*, and *κ* are entangled in intricate trade-offs; nonetheless, the current BO framework adaptively optimizes these parameters using minimal experimental iterations.

Discussion

We proposed III–V compound semiconductor thin films as thermoelectric thin films and improved the performance of Sn-doped $In_{1-x}Ga_xAs_{1-y}Sb_y$ using machine learning. BO was suitable for the rapid identification of the growth conditions that maximized *ZT* (0.033), and the maximum value of *ZT* was approximately three times greater than that of the initial sample. This outcome demonstrated the efficacy of the BO model in understanding the fundamental behaviors of the thermoelectric properties of III–V compound semiconductors. The GPR algorithm, which employed material properties as inputs, conclusively revealed that high In composition and low T_{sub} were particularly effective at increasing *ZT*. The optimal substrate temperature ($T_{sub} = 205$ °C) showed the potential for depositing InGaAsSb thermoelectric thin films onto plastic substrates. Therefore, we demonstrated the efficacy of BO in enhancing the properties of multi-component thermoelectric materials characterized by diverse and intricate parameter relationships.

Methods

Sample preparation with BO optimization

Sn-doped $In_{1-x}Ga_xAs_{1-y}Sb_y$ films (thickness: 500 nm) were deposited onto SiO_2 glass substrates using a vacuum evaporation system equipped with Knudsen cells. Using BO, we investigated the optimum cell temperatures for Ga, As, Sb, and Sn ($T_{Ga\text{-cell}} = 820$–970 °C, $T_{As\text{-cell}} = 150$–225 °C, $T_{Sb\text{-cell}} = 300$–450 °C, and $T_{Sn\text{-cell}} = 600$–1000 °C) and the substrate temperature ($T_{sub} = 100$–600 °C). The In-cell temperature was varied from 635 °C to 775 °C depending on the $T_{Ga\text{-cell}}$ used to maintain a film thickness of 500 nm. The deposition time was fixed at 1 h. We executed BO using a GPR algorithm in the Python library GPyOpt[41–43], with *EI* as the

acquisition function. The 1st–5th cycles of BO training data were randomly created.

Sample evaluation

The samples were examined using a SEM (Hitachi-high-tech SU7000, voltage: 15 kV). In the SEM system, the compositions of $In_{1-x}Ga_xAs_{1-y}Sb_y$ were determined from the EDX spectra obtained in 25 μm squares. SIMS measurements were conducted to determine the Sn concentration using a PHI ADEPT1010 instrument. The out-of-plane XRD patterns were obtained using a diffractometer (Rigaku SmartLab) equipped with a Ge monochromator (wavelength: 1.54 Å) and a Cu-Kα radiation source (voltage: 40 kV, current: 30 mA). The incident angle was varied from 20 ° to 60 ° in steps of 0.01 °. Hall effect measurements were obtained via the van der Pauw method using a Lake Shore M91-EV system, where n and μ were averaged over ten measurements for each sample. The σ and S values were measured using a ZEM-3 system, in which Ag paste was used to fix the sample to a ceramic stage[44,45]. The cross-plane κ was measured using a PicoTherm PicoTR.

Acknowledgements
This study was financially supported by the JST FOREST (No. JPMJFR222J), JSPS KAKENHI (Nos. 21H01358 and 23KJ0271), the TEPCO Memorial Foundation, and the JACI Prize for Encouraging Young Researchers. The authors are grateful to Prof. T. Sekiguchi (University of Tsukuba) for the SEM and EDX measurements. Some experiments were conducted at the Advanced Research Infrastructure for Materials and Nanotechnology in Japan.

Author contributions
T.I. and K.T. conceived and designed the study. T.I., K.N., and T.N. fabricated the sample and performed the analyses. T.I. implemented the BO program. K.T. and T.S. managed and supervised the study. All authors discussed the results and commented on the manuscript.

Data availability
The data supporting the findings of this study are available upon reasonable request from the authors.

Competing interests
The authors declare no competing interests.

Supplementary information The online version contains supplementary material available at https://doi.org/10.1038/s41427-024-00536-w.

Received: 1 November 2023 Revised: 31 January 2024 Accepted: 2 February 2024
Published online: 29 March 2024

References

1. Gholikhania, M., Roshanib, H., Dessoukya, S. & Papagiannakis, A. T. A critical review of roadway energy harvesting technologies. *Appl. Energy* **261**, 114388 (2020).
2. Akinaga, H. Recent Advances and Future Prospects in Energy Harvesting Technologies. *Jpn. J. Appl. Phys.* **59**, 110201 (2020).
3. Petsagkourakis, I. et al. Thermoelectric materials and applications for energy harvesting power generation. *Sci. Technol. Adv. Mater.* **19**, 836 (2018).
4. Bahk, J. H., Fang, H., Yazawa, K. & Shakouri, A. Flexible Thermoelectric Materials and Device Optimization for Wearable Energy Harvesting. *J. Mater. Chem. C* **3**, 10362–10374 (2015).
5. Venkatasubramanian, R., Siivola, E., Colpitts, T. & O'Quinn, B. Thin-film thermoelectric devices with high room-temperature figures of merit. *Nature* **413**, 597–602 (2001).
6. Bharti, M., Singh, A., Samanta, S. & Aswal, D. K. Conductive polymers for thermoelectric power generation. *Prog. Mater. Sci.* **93**, 270–310 (2018).
7. Nakwaski, W. Thermal conductivity of binary, ternary, and quaternary III-V compounds. *J. Appl. Phys.* **64**, 159–166 (1988).
8. Adachi, S. Lattice thermal resistivity of III–V compound alloys. *J. Appl. Phys.* **54**, 1844–1848 (1983).
9. Pei, Y. & Morelli, D. T. Vacancy phonon scattering in thermoelectric In_2Te_3-InSb solid solutions. *Appl. Phys. Lett.* **94**, 122112 (2009).
10. Yamaguchi, S., Matsumoto, T., Yamazaki, J., Kaiwa, N. & Yamamoto, A. Thermoelectric properties and figure of merit of a Te-doped InSb bulk single crystal. *Appl. Phys. Lett.* **87**, 201902 (2005).
11. Cui, J. L. et al. Cu addition and its role in thermoelectric properties and nanostructuring in the series compounds $(InSb)_nCu_m$. *Curr. Appl. Phys.* **12**, 69–74 (2012).
12. Bowers, R., Ure, R. W. Jr., Bauerle, J. E. & Cornish, A. J. InAs and InSb as Thermoelectric Materials. *J. Appl. Phys.* **30**, 930–934 (1959).
13. Mingo, N. Thermoelectric figure of merit and maximum power factor in III–V semiconductor nanowires. *Appl. Phys. Lett.* **84**, 2652 (2004).
14. Rode, D. L. Electron transport in InSb, InAs, and InP. *Phys. Rev. B* **3**, 3287–3299 (1971).
15. Kumar, V. N., Hayakawa, Y., Udono, H. & Inatomi, Y. Enhanced thermoelectric properties of InSb: Studies on In/Ga doped GaSb/ InSb crystals. *Intermetallics* **105**, 21–28 (2019).
16. Zhang, Q. et al. Enhanced thermoelectric performance in $In_{1-x}Ga_xSb$ originating from the scattering of point defects and nanoinclusion. *J. Mater. Chem.* **21**, 12398–12401 (2011).
17. Kumar, V. N., Hayakawa, Y., Udono, H. & Inatomi, Y. An Approach to Optimize the Thermoelectric Properties of III-V Ternary InGaSb Crystals by Defect Engineering via Point Defects and Microscale Compositional Segregations. *Inorg. Chem.* **58**, 11579–11588 (2019).
18. Kumar, V. N. et al. Effects of varying indium composition on the thermoelectric properties of $In_xGa_{1-x}Sb$ ternary alloys. *Appl. Phys. A* **122**, 885 (2016).
19. Kanarik, K. J. et al. Human–machine collaboration for improving semiconductor process development. *Nature* **616**, 707–711 (2023).
20. Ueno, T., Rhone, T. D., Hou, Z., Mizoguchi, T. & Tsuda, K. COMBO: An efficient Bayesian optimization library for materials science. *Materials. Discovery* **4**, 18–21 (2016).
21. Miyagawa, S., Gotoh, K., Kutsukake, K., Kurokawa, Y. & Usami, N. Application of Bayesian optimization for improved passivation performance in TiO_x/SiO_y/c-Si heterostructure by hydrogen plasma treatment. *Appl. Phys. Express* **14**, 025503 (2021).
22. Osada, K. et al. Adaptive Bayesian optimization for epitaxial growth of Si thin films under various constraints. *Mater. Today Commun.* **25**, 101538 (2020).
23. Wakabayashi, Y. K. et al. Machine-learning-assisted thin-film growth: Bayesian optimization in molecular beam epitaxy of $SrRuO_3$ thin films. *APL Mater* **7**, 101114 (2019).
24. Ohkubo, I. et al. T. Realization of closed-loop optimization of epitaxial titanium nitride thin-film growth via machine learning. *Materials Today Physics* **16**, 100296 (2021).
25. Will-Cole, A. R. et al. N. X. Application of Bayesian Optimization and Regression Analysis to Ferromagnetic Materials Development. *IEEE Trans. Magn.* **58**, 1–8 (2022).
26. Siemenn, A. E., Ren, Z., Li, Q. & Buonassisi, T. Fast Bayesian optimization of Needle-in-a-Haystack problems using zooming memory-based initialization (ZoMBI). *NPJ Comput. Mater.* **9**, 79 (2023).
27. Rustam, S. et al. Optimization of Thermal Conductance at Interfaces Using Machine Learning Algorithms. *ACS Appl. Mater. Interfaces.* **14**, 32590–32597 (2022).
28. Ju, S. et al. Designing Nanostructures for Phonon Transport via Bayesian Optimization. *Phys. Rev. X.* **7**, 021024 (2017).

29. Wang, Z., Funada, T., Onda, T. & Chen, Z. Knowledge extraction and performance improvement of Bi_2Te_3-based thermoelectric materials by machine learning. *Mater. Today Phys.* **31**, 100971 (2023).
30. Shang, W. et al. Hybrid Data-driven Discovery of High-performance Silver Selenide-based Thermoelectric Composites. *Adv. Mater.* **Jul 26**, e2212230 (2023).
31. Chiba, N., Masuda, K., Uchida, K. & Miura, Y. Designing composition ratio of magnetic alloy multilayer for transverse thermoelectric conversion by Bayesian optimization. *APL. Mach. Learn.* **1**, 026114 (2023).
32. Saito, M. et al. Solid-phase crystallization of gallium arsenide thin films on insulators. *Mater. Sci. Semicond. Process.* **124**, 105623 (2021).
33. Tomisu, M., Inoue, N. & Yasuoka, Y. Annealing effect of vacuum evaporated InSb thin films. *Vacuum* **47**, 239–242 (1996).
34. Senthilkumar, V. et al. Characterization of p-type In-Sb thin films prepared by vacuum evaporation. *Vacuum* **79**, 163–170 (2005).
35. Takushima, M., Kajikawa, Y., Kuya, Y., Shiba, M. & Ohnishi, K. Low-Temperature Growth of InAs on Glass and Plastic Film Substrates by Molecular-Beam Deposition. *Jpn. J. Appl. Phys.* **47**, 1469–1472 (2008).
36. Kajikawa, Y., Okuzako, T., Takami, S. & Takushima, M. Electrical properties of polycrystalline GaInAs thin films. *Thin Solid Films* **519**, 136–144 (2010).
37. Dutta, P. S., Bhat, H. L. & Kumar, V. The physics and technology of gallium antimonide: An emerging optoelectronic material. *J. Appl. Phys.* **81**, 5821–5870 (1997).
38. Noguchi, M., Hirakawa, K. & Ikoma, T. Intrinsic electron accumulation layers on reconstructed clean InAs(100) surfaces. *Phys. Rev. Lett.* **66**, 2243 (1991).
39. Compeán-Jasso, V. H. et al. Sn doped GaSb grown by liquid phase epitaxy. *Thin Solid Films* **548**, 168–170 (2013).
40. Harrison, R. J. & Houston, P. A. LPE growth and characterization of n-type InAs. *J. Cryst. Growth.* **78**, 257–262 (1986).
41. González, J., Osborne, M. & Lawrence, N. D. GLASSES: relieving the myopia of Bayesian optimisation. In: *Proc. 19th International Conference on Artificial Intelligence and Statistics (AISTATS)* 790–799 (PMLR, 2016).
42. González, J., Dai, Z., Hennig, P. & Lawrence, N. D. Batch Bayesian optimization via local penalization. In *Proc. 19th International Conference on Artificial Intelligence and Statistics (AISTATS)* 648–657 (PMLR, 2016).
43. González, J., Longworth, J., James, D. & Lawrence, N. Bayesian Optimization for synthetic gene design. Preprint at https://arxiv.org/abs/1505.01627 (2014).
44. Kusano, K., Yamamoto, A., Nakata, M., Suemasu, T. & Toko, K. Thermoelectric Inorganic SiGe Film Synthesized on Flexible Plastic Substrate. *ACS Appl. Energy Mater* **1**, 5280–5285 (2018).
45. Ozawa, T., Imajo, T., Suemasu, T. & Toko, K. High thermoelectric power factors in polycrystalline germanium thin films. *Appl. Phys. Lett.* **119**, 132101 (2021).